Measuring Gravity Wave Parameters from a Nighttime Satellite Low-Light Image Based on Two-Dimensional Stockwell Transform

SHENSEN HU, SHUO MA, AND WEI YAN

College of Meteorology and Oceanology, National University of Defense Technology, Nanjing, China

NEIL P. HINDLEY

Centre for Space, Atmospheric and Oceanic Sciences, University of Bath, Bath, United Kingdom

KAI XU

No. 92877 Troop, People's Liberation Army, Zhoushan, China

JUN JIANG

Institute of Applied Meteorology, Beijing, China

(Manuscript received 12 June 2018, in final form 11 September 2018)

ABSTRACT

Atmospheric gravity waves are a kind of mesoscale disturbance, commonly found in the atmospheric system, that plays a key role in a series of mesospheric dynamic processes. When propagating to the upper atmosphere, the gravity waves will disturb the local temperature and density, and then modulate the intensity of the surrounding airglow radiation. As a result, the presence of gravity waves on a moonless night can usually cause the airglow to reveal ripple features in low-light images. In this paper we have applied a two-dimensional Stockwell transform technique (2DST) to airglow measurements from nighttime low-light images of the day–night band on the *Suomi National Polar-Orbiting Partnership*. To our knowledge this study is the first to measure localized mesospheric gravity wave brightness amplitudes, horizontal wavelengths, and propagation directions using such a method and data. We find that the method can characterize the general shape and amplitude of concentric gravity wave patterns, capturing the dominant features and directions with a good degree of accuracy. The key strength of our 2DST application is that our approach could be tuned and then automated in the future to process tens of thousands of low-light images, globally characterizing gravity wave parameters in this historically poorly studied layer of the atmosphere.

1. Introduction

Internal atmospheric gravity waves are oscillations that result from an air parcel being vertically displaced from an equilibrium state. These gravity waves are a kind of mesoscale disturbance, commonly found in the atmospheric system, that plays a key role in a series of mesospheric dynamic processes. They have important influences on the transmission of atmospheric energy and momentum from bottom to top (Holton 1983; Fritts and Alexander 2003). In the past few decades, gravity waves have attracted considerable research attention all over the world. However, the description of gravity waves in the study of global-scale climate models is parameterized because many waves or wave sources are often subgrid-scale phenomena, so they are not well resolved. But these parameterizations are often poorly constrained for lack of real gravity wave observations (Alexander et al. 2010; Geller et al. 2013). Therefore, accurate measurement of gravity wave parameters is of great significance for the development of current and even next-generation global climate models.

The satellite observation data from imaging instruments can globally obtain the characteristics of gravity waves spanning hundreds of kilometers, which provides us with a unique perspective to observe gravity waves. Gravity wave observations based on a variety of satellite data have made great progress in recent years, and they have greatly

Corresponding author: Dr. Shuo Ma, mashuo_2016@163.com

DOI: 10.1175/JTECH-D-18-0092.1

expanded our understanding of gravity waves (Alexander et al. 2009; Hoffmann et al. 2013; Nishioka et al. 2013; Azeem et al. 2015).

The *Suomi National Polar-Orbiting Partnership* (*Suomi NPP*) has become a new generation of operational polar-orbiting meteorological environmental satellite since it was launched in 2011 (Hillger et al. 2013). From its 824-km orbital altitude, the *Suomi NPP* completes an orbit in ~102 min, thus providing global coverage ~14 times every day. The Visible Infrared Imaging Radiometer Suite (VIIRS) on board the spacecraft has a strong capability of environmental detection with its 22 spectral channels (Miller et al. 2013). The day–night band (DNB) of VIIRS covering a wide band of 0.5–0.9 μm has a nearly constant spatial resolution. It images the Earth scenes not only at traditional daytime but also at night with weak moonlight or starlight (Uprety et al. 2013; Ma et al. 2015, 2016; Hu et al. 2018). On moonless nights, the DNB can even detect pretty weak radiation airglow located in the mesopause (Miller et al. 2013). When propagating to the upper atmosphere, gravity waves will disturb the local temperature and density, and then modulate the intensity of the surrounding airglow radiation. As a result, the presence of gravity waves on a moonless night can usually cause the airglow to have distinct ripple features in low-light images (Miller et al. 2015). Lai et al. (2017) validated the gravity waves observed by DNB images with the help of thermal infrared data from VIIRS and wind speed data from Modern-Era Retrospective Analysis for Research and Applications. They concluded that these gravity waves had sources that included orography, thunderstorm, typhoon, and baroclinic instability.

Mesoscale numerical models, such as the three-dimensional mesoscale model (Dudhia 1993) and the Weather Research and Forecasting Model (Skamarock et al. 2005), are often used to study the characteristics of gravity waves (Kuester et al. 2008; Plougonven et al. 2008; Kim et al. 2009). However, since the mesoscale models rarely extend into the mesosphere, the gravity wave parameters observed in DNB images cannot be easily simulated in these mesoscale models.

In this paper we present a processing algorithm for measuring gravity wave parameters from a nighttime satellite low-light image via the two-dimensional Stockwell transform method. Section 2 introduces the data and spectral methods used. Section 3 describes the whole processing algorithm of measuring gravity wave parameters from DNB images. Section 4 shows the experimental results dealing with gravity waves induced by Typhoon Manhasen on 13 and 14 May 2013. Conclusions are provided in section 5.

2. Data and spectral methods

a. Data

In this paper the DNB channel product SVDNB released by the NOAA Comprehensive Large Array-Data Stewardship System (CLASS) is used. The VIIRS DNB sensor data record (SDR; SVDNB) product belongs to SDR-level products, providing the radiance information of the Earth scene.

The spectral range of the DNB channel is 0.5–0.9 μm. The DNB data have been calibrated with high radiometric precision, and even the high-gain stage used at night has a recognized radiometric calibration uncertainty of 15% (1σ). With the constant 742-m spatial resolution, DNB images can reveal many details of mesoscale gravity waves. Since the intensity of the nighttime airglow radiation is much lower than that of the moon, the existence of moon radiation will greatly influence the observability of gravity waves (Miller et al. 2012). Therefore, only on moonless nights can it be possible to observe gravity wave patterns in DNB images.

b. The Stockwell transform

For a smoothly varying, continuous, and one-dimensional function of time $h(t)$, the generalized analytical form of the Stockwell transform (S transform) (Stockwell et al. 1996; Stockwell 1999) is given as

$$S(\tau, f) = \int_{-\infty}^{\infty} h(t)\omega_g(t-\tau, f)e^{-i2\pi ft}\,dt, \tag{1}$$

where τ is translation in the time domain and f is frequency; $\omega_g(t-\tau, f)$ is a windowing function scaled with frequency, taking the traditional form of the normalized Gaussian window

$$\omega_g(t-\tau, f) = \frac{1}{\sigma\sqrt{2\pi}}e^{-(t-\tau)^2/2\sigma^2}, \tag{2}$$

where σ is the standard deviation.

Equation (1) can be rewritten as a more explicit form,

$$S(\tau, f) = \frac{|f|}{c\sqrt{2\pi}}\int_{-\infty}^{\infty} h(t)e^{-(t-\tau)^2f^2/2c^2}e^{-i2\pi ft}\,dt, \tag{3}$$

where c is the scaling parameter, usually set to 1. But it may also take other values to achieve more specific time–frequency localization requirements (Mansinha et al. 1997; Fritts et al. 1998; Pinnegar and Mansinha 2003; Hindley et al. 2016).

The time-domain convolution can be written as a frequency-domain multiplication to reduce the computational costs (Stockwell et al. 1996),

$$S(\tau,f)=\int_{-\infty}^{\infty}H(\alpha+f)e^{-2\pi^2c^2\alpha^2/f^2}e^{i2\pi\alpha\tau}\,d\alpha, \qquad (4)$$

where α is translation in the frequency domain and $H(\alpha+f)$ is a shifted version of $H(f)$, which is in turn the frequency analog of $H(t)$. The frequency-domain form of the voice Gaussian is given as

$$\omega_g(\alpha,f)=e^{-2\pi^2c^2\alpha^2/f^2}. \qquad (5)$$

c. The two-dimensional S transform

The S-transform can be easily extended to higher dimensions based on the one-dimensional form (Mansinha et al. 1997; Hindley et al. 2016). For a given two-dimensional image $h(x, y)$, the two-dimensional Stockwell transform (2DST) is given as

$$S(\tau_x,\tau_y,f_x,f_y)=\int_{-\infty}^{\infty}\int_{-\infty}^{\infty}h(x,y)\times\frac{|f_x||f_y|}{2\pi c^2}e^{-\left\{\left[(x-\tau_x)^2f_x^2+(y-\tau_y)^2f_y^2\right]/2c^2\right\}}e^{-i2\pi(f_xx+f_yy)}\,dx\,dy, \qquad (6)$$

where τ_x, τ_y are translation in the x and y directions, respectively. Note that f_x and f_y are simple spatial frequencies, inverse of wavelength. However, the notation of angular wavenumber is more commonly used in the atmospheric sciences, in the form of $k_x=2\pi f_x$, $k_y=2\pi f_y$. Therefore, the 2DST can be written in terms of angular wavenumber,

$$S(\tau_x,\tau_y,k_x,k_y)=\int_{-\infty}^{\infty}\int_{-\infty}^{\infty}h(x,y)\times\frac{|k_x||k_y|}{8\pi^3c^2}e^{-\left\{\left[(x-\tau_x)^2f_x^2+(y-\tau_y)^2f_y^2\right]/8\pi^2c^2\right\}}e^{-i(k_xx+k_yy)}\,dx\,dy. \qquad (7)$$

The two-dimensional form of the Gaussian windowing term is

$$\omega_g(x,y,k_x,k_y)=\frac{|k_x||k_y|}{8\pi^3c^2}e^{-(k_x^2x^2+k_y^2y^2)/8\pi^2c^2}, \qquad (8)$$

where c is a scaling parameter.

Similarly, the frequency-domain multiplication can achieve greater computational efficiency,

$$S(\tau_x,\tau_y,k_x,k_y)=\int_{-\infty}^{\infty}\int_{-\infty}^{\infty}H(\alpha_x+k_x,\alpha_y+k_y)\times\frac{1}{4\pi^2}e^{-\left[(2\pi^2c^2\alpha_x^2/k_x^2)+(2\pi^2c^2\alpha_y^2/k_y^2)\right]}e^{i(\alpha_x\tau_x+\alpha_y\tau_y)}\,dx\,dy, \qquad (9)$$

where $H(\alpha_x+k_x, \alpha_y+k_y)$ is a shifted version of $H(\alpha_x, \alpha_y)$, which is in turn the wavenumber analog of the input image. The frequency-domain form of the voice Gaussian is given as

$$\omega_g(\alpha_x,\alpha_y,k_x,k_y)=e^{-[(2\pi^2c^2\alpha_x^2/k_x^2)+(2\pi^2c^2\alpha_y^2/k_y^2)]}. \qquad (10)$$

The 2DST has been discussed and applied in a variety of fields since it was first introduced. Hindley et al. (2016) used it for the purpose of gravity wave analysis from two-dimensional data in the atmospheric sciences at the first time. Similarly, the 2DST could be used for the gravity analysis from DNB images after some steps are done. In the following section, we describe our implementation algorithm to measure gravity wave parameters from two-dimensional DNB data.

3. Algorithm

a. Data selection and preprocessing

The SVDNB data product consisting of four granules can be turned into an image of 3072 × 4064 pixels, with a width of ~3000 km. Therefore, gravity waves as a mesoscale atmospheric phenomenon cover only a small part of the observation area. There is no need to process all the data because of the huge computation cost. For a low-light image with localized typical gravity wave features, a certain range of data revealing the gravity wave information is usually selected for processing.

Human lights have a great influence on the observation of gravity waves with the DNB and are usually continuous and widespread. As a result, it is quite difficult to totally eliminate the effects of human lights.

Therefore, the best data to use are those over the oceans far away from land, despite the existence of other light sources, such as lightning and fishing boats.

On moonless nights the moonlight radiation reflected by the ground is weak enough to be neglected, and the typical DNB radiance is in the range of 10^{-9}–10^{-11} W cm^{-2} sr^{-1}. Since it is the relative radiance between neighboring pixels that matters rather than the absolute radiance values, all selected data are multiplied by 10^{10} in the calculation codes for the convenience of data processing.

In general, the absolute intensity of airglow radiation is relatively small. Therefore, after the product operation, the bright pixels with radiance larger than 10^{-9} W cm^{-2} sr^{-1} are considered as human lights or natural lights such as lightning, whose radiance can reach a fairly high level. To better observe the radiance distribution of the low-light data, all pixels with radiance greater than 10^{-9} W cm^{-2} sr^{-1} are all set to this value as the upper limit of radiance.

b. *Removal and inpainting of lightning pixels*

For the gravity waves induced by tropical storms, there is often lightning in nearby areas at the same time. As a traditional scanning radiometer, DNB was not designed for the purpose of lightning monitoring. However, if there is a high generation probability and a long duration of storm, DNB has the capability of detecting the cloud-top diffuse lights of the lightning (Bankert et al. 2011). In the data selection step, the original data have been selected to avoid the interference of wide-ranging human lights. Therefore, lightning is the major influence factor in the process of gravity wave identification.

Since the 16 adjacent detectors of DNB scan lightning at the same time, there is a bright 16-pixel-wide streak along the scan line. To process the low-light images containing lightning information, we applied a convolution kernel as a directional filter, taking the form of 11×3 pixels in Table 1.

Through the convolution calculation, the upper- and lower-edge pixels of the lightning streak will have significantly higher values than the inner ones. Therefore, the position of the lightning pixels can be effectively obtained by setting a certain threshold.

Lightning pixels are usually seen as wide streaks from DNB images. The inpainting effects using a simple image interpolation method are not satisfactory. For the void areas left after the removal of lightning pixels, curvature-driven diffusion (CDD) image restoration technology (Chan and Shen 2001) is used to fill in the pixels. The CDD model is proposed by introducing the curvature-driven algorithm on the basis of the total variation (TV) model (Rudin et al. 1992), solving the problem of visual connectivity of images effectively.

TABLE 1. The convolution kernel used as a directional filter.

−1	−1	−1	−1	−1	−1	−1	−1	−1	−1	−1
2	2	2	2	2	2	2	2	2	2	2
−1	−1	−1	−1	−1	−1	−1	−1	−1	−1	−1

In addition, individual fishing boat lights at night are often observed in the ocean, which are much brighter than the surrounding dark background pixels. For a single fishing boat light pixel with a peak radiance, a satisfactory result could be obtained by taking the average value of the surrounding pixels for interpolation.

In this section the purpose of removing and repairing lightning pixels in DNB images is to reduce the influence of peak values on the 2DST. Therefore, when setting the threshold for lightning identification, the algorithm should cover as many potential lightning pixels as possible. There is no doubt that such a threshold-setting strategy may consider some nonlightning pixels as lightning pixels. However, repairing a small number of discrete nonlightning pixels will not affect the holistic radiance distribution greatly.

c. *Using the 2DST method*

Compared with the radiance data, the radiance perturbation data can effectively remove the limb brightening effect and other large-scale satellite radiance fluctuations. Therefore, the distribution characteristics of gravity wave energy and momentum can be better revealed. After the removal and inpainting of the lightning pixels, the radiance perturbation distribution is then extracted from radiance data via a fourth-order polynomial fit along the scan line (Wu 2004; Alexander and Barnet 2007).

On moonless nights, the signal-to-noise ratio (SNR) of DNB data is quite low, making random noise unneglectable. And the spatial resolution of DNB is much smaller than the typical horizontal wavelength of gravity waves. Therefore, the radiance disturbance data can be smoothed to reduce the interference of random noise. By adjusting the parameter settings, the Gaussian smoothing method is used and then gravity wave features are highlighted in the image.

We now compute the 2DST of the smoothed radiance perturbation data. From this we obtain a complete four-dimensional object containing a localized two-dimensional spectrum for each location in the two-dimensional image. There is a two-dimensional image of complex-valued localized spectral coefficients, indicating the absolute magnitude of waves with wavenumbers k_x and k_y at the given location. A single dominant wave for each location is

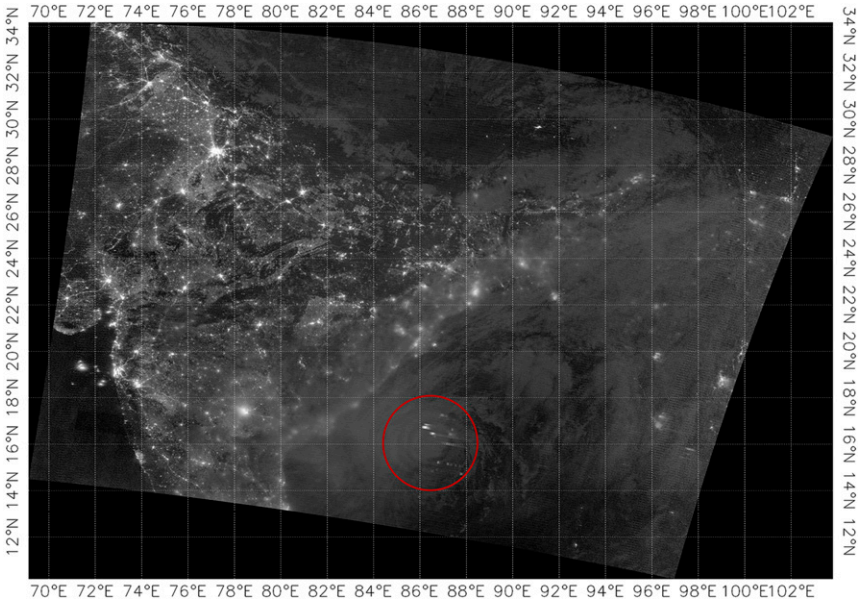

FIG. 1. The DNB low-light image at 1953 UTC 14 May 2013 with the gravity waves circled in red.

identified to determine the two-dimensional complex-valued spectral peak coefficients, which has the same size as the input image (Hindley et al. 2016).

At the same time, the wavenumbers k_x and k_y can be obtained from the location of the spectral peak coefficients. Therefore, three 2D parameters can be produced at each location in the original images, which are the spectral peak coefficients and the two wavenumbers in both directions.

Taking the real part of the complex-valued images containing the dominant coefficients, we can recover a "reconstruction" of the waves. With the help of two wavenumbers, the horizontal wavelength of the dominant wave at each location can be obtained by

$$\lambda_H(\tau_x, \tau_y) = [k_x(\tau_x, \tau_y)^2 + k_y(\tau_x, \tau_y)^2]^{-1/2}. \quad (11)$$

The direction of wave propagation is denoted by the degrees counterclockwise from the x axis of the along-scan direction, which can be determined by

$$\theta(\tau_x, \tau_y) = \arctan\left[\frac{k_x(\tau_x, \tau_y)}{k_y(\tau_x, \tau_y)}\right]. \quad (12)$$

Note that the propagation direction is subject to a $\pm\pi$ radian ambiguity, which is unavoidable for the lack of a priori or extra dimensional information, such as time.

Following the processing algorithm, the distribution of the horizontal wavelength and the propagation direction of gravity waves can be finally measured from the released original DNB data.

4. Experimental results

a. *Experimental results of 14 May 2013*

On 14 May 2013, Tropical Cyclone Manhasen was moving northeast in the southern Bay of Bengal in the Indian Ocean. Yue et al. (2014) found that a group of concentric gravity waves induced by the storm were observed from the DNB low-light image. The center of gravity waves was located near 16°N, 87°E, and the horizontal wavelength was roughly estimated to be ~60 km by the pixel numbers. To validate our experimental results to some extent, the SVDNB product at 1953 UTC 14 May 2013 was used, shown in Fig. 1.

The 701 × 901-pixel area near the gravity wave center is selected to measure local gravity wave parameters. From Fig. 2 it can be seen that there are many bright streaks in the middle caused by lightning. The lengths of these bright streaks are quite different. The shorter ones are only few pixels long, while the longer ones may span hundreds of pixels. However, the widths of both sets of streaks are equal to 16 pixels, the same as the number of DNB detectors. In addition, the inner pixels are much brighter than those outside along the vertical direction.

By the directional filter of the abovementioned convolution kernel, the lightning pixels are identified using a threshold and then removed. The CDD model is used to repair the void areas left. As shown in Fig. 3, the majority of bright lightning pixels in Fig. 2 have been processed well. In general, the image inpainting result is good enough to

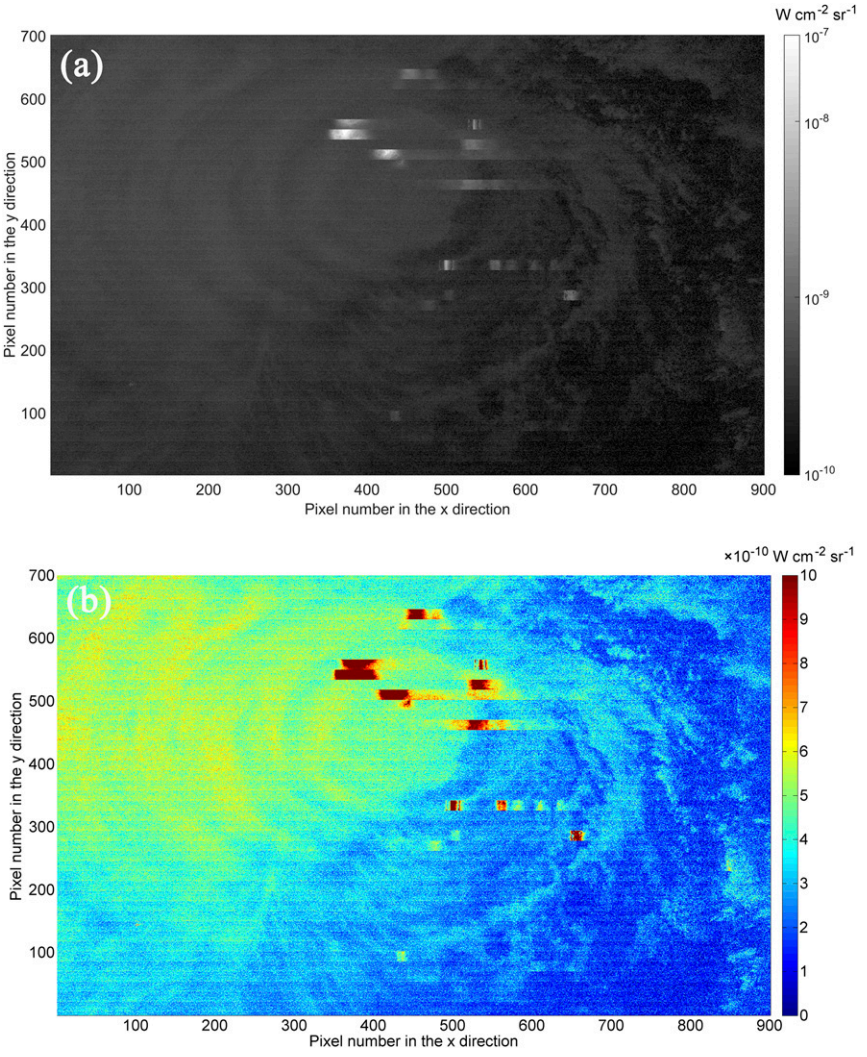

FIG. 2. The local DNB data intercepted on 14 May: (a) the grayscale image after logarithmic operation on radiance and (b) the pseudocolor image.

continue the subsequent steps, though there are still a few lightning pixels revealing the traces of restoration.

The ripple structure of gravity waves is clear enough to be observed by eye, and the center of the wave field can be easily identified. However, the poor contrast of Fig. 3 may result in a relatively blurry visual effect for the gravity wave observation. For the ripples in the upper-left area, the value of high-value pixels is near $7 \times 10^{-10}\,\mathrm{W\,cm^{-2}\,sr^{-1}}$, while that of low-value pixels is near $4 \times 10^{-10}\,\mathrm{W\,cm^{-2}\,sr^{-1}}$. For the ripples in the lower-right area, the value of the high-value pixels is near $4 \times 10^{-10}\,\mathrm{W\,cm^{-2}\,sr^{-1}}$, while that of low-value pixels is near $1 \times 10^{-10}\,\mathrm{W\,cm^{-2}\,sr^{-1}}$. The upper-left area is much brighter than the lower-right area. Therefore, the 2DST calculation result will be seriously affected, as the two examples are processed in one image.

Figure 4 shows the radiance perturbation data calculated via a fourth-order fit along the horizontal direction on the basis of radiance data. Compared with Fig. 3, the radiance perturbation data for the entire image is generally more balanced by subtracting the background radiance, eliminating the large-scale variation trend of radiance effectively. On the whole, the pixels in the image now reveal distinct ripple features alternating with brightness and darkness, which can help identify the structure of gravity waves better.

The median filter and Gaussian smoothing method are performed on the radiance perturbation data. As shown in Fig. 5, the influence of random noise between neighboring pixels is reduced by smoothing effectively, making the image characteristics of gravity waves clearer.

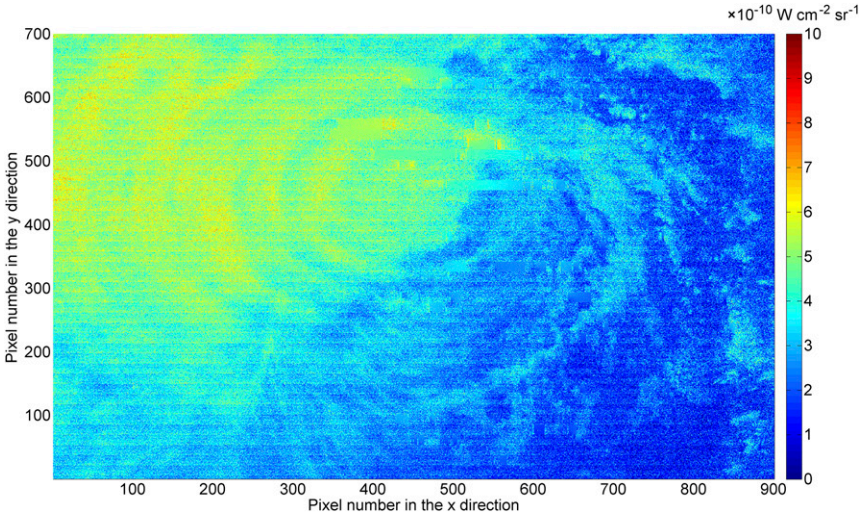

FIG. 3. The radiance distribution after image inpainting.

Finally, in accordance with the aforementioned method in section 3c, the 2DST is performed based on the smoothed radiance perturbation data, and the calculation result is shown in Fig. 6. Figure 6a shows the original smoothed radiance perturbation input into the transformation model. Figure 6b is the real amplitude of the data. The reconstructed gravity waves generally reveal the image characteristics of concentric gravity waves, except for some certain areas mistaken as a result of poor SNR. Figure 6c is the distribution of the absolute amplitude: the brighter the pixels, the larger the absolute amplitude of the area. It can be seen that the upper-right area in the figure has stronger gravity wave features. Figure 6d shows the horizontal wavelength distribution of gravity waves as well as the contour lines of absolute amplitude. The horizontal wavelengths are mainly concentrated in the range of 40–70 km, which is generally consistent with the naked eye estimation result of 60 km in Yue et al. (2014), taking the product of the number of pixels and the DNB spatial resolution. The areas of much longer wavelengths are just the areas of poor SNR in Fig. 6b. Figure 6e shows the propagation direction of gravity waves, defined by the degrees counterclockwise from the x axis, as well as the contour lines of absolute amplitude. It can be seen that the distribution of the propagation direction is generally divided into four parts. In the lower-left and upper-right areas, the angle of the propagation direction is positive,

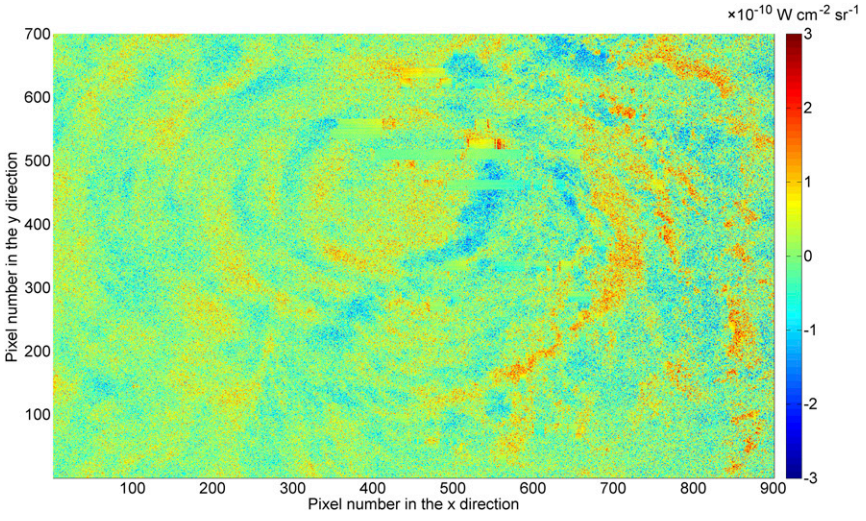

FIG. 4. The radiance perturbation distribution.

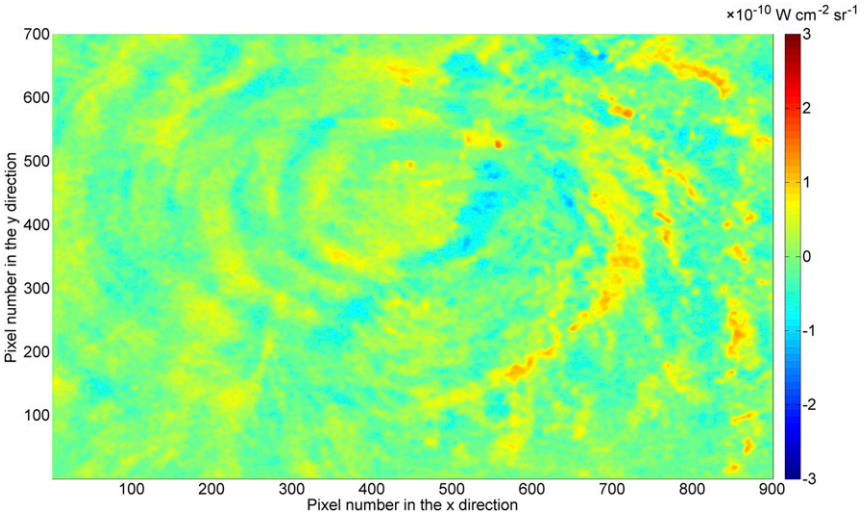

FIG. 5. The smoothed radiance perturbation distribution.

while in the upper-left and lower-right areas of the figure, the angle of the propagation direction is negative, which is consistent with the characteristics of the concentric gravity waves.

b. *Experimental results of 13 May 2013*

As a polar-orbiting meteorological environment satellite, the *Suomi NPP* usually passes over the same place only twice a day. Therefore, there is only one chance every night to acquire the local low-light image of a certain region. Fortunately, the gravity waves induced by Manhasen can also be found in the DNB image of the night before. The center of the gravity waves was located near 13°N, 85°E, and the intensity, structure, and other characteristics on that night were all different from those on 14 May.

Similarly, for the low-light image of 2016 UTC 13 May 2013, we used the method described in section 3 to study the characteristics of gravity waves and to measure the gravity wave parameters.

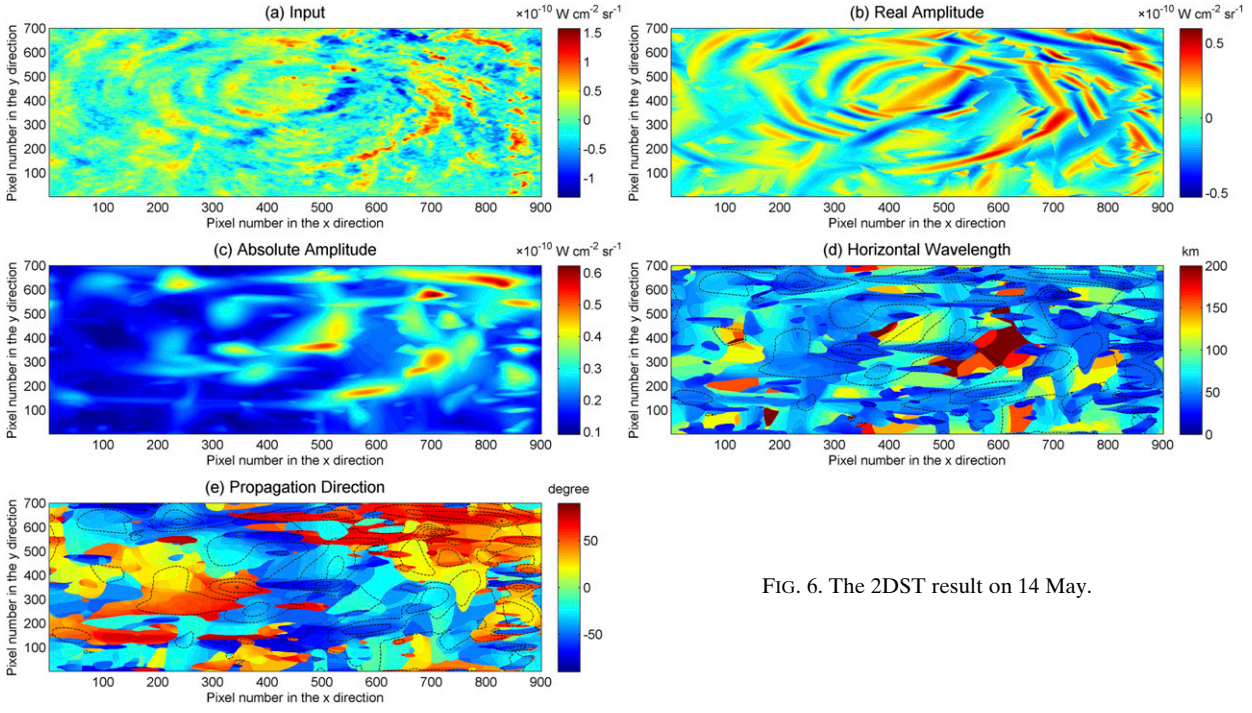

FIG. 6. The 2DST result on 14 May.

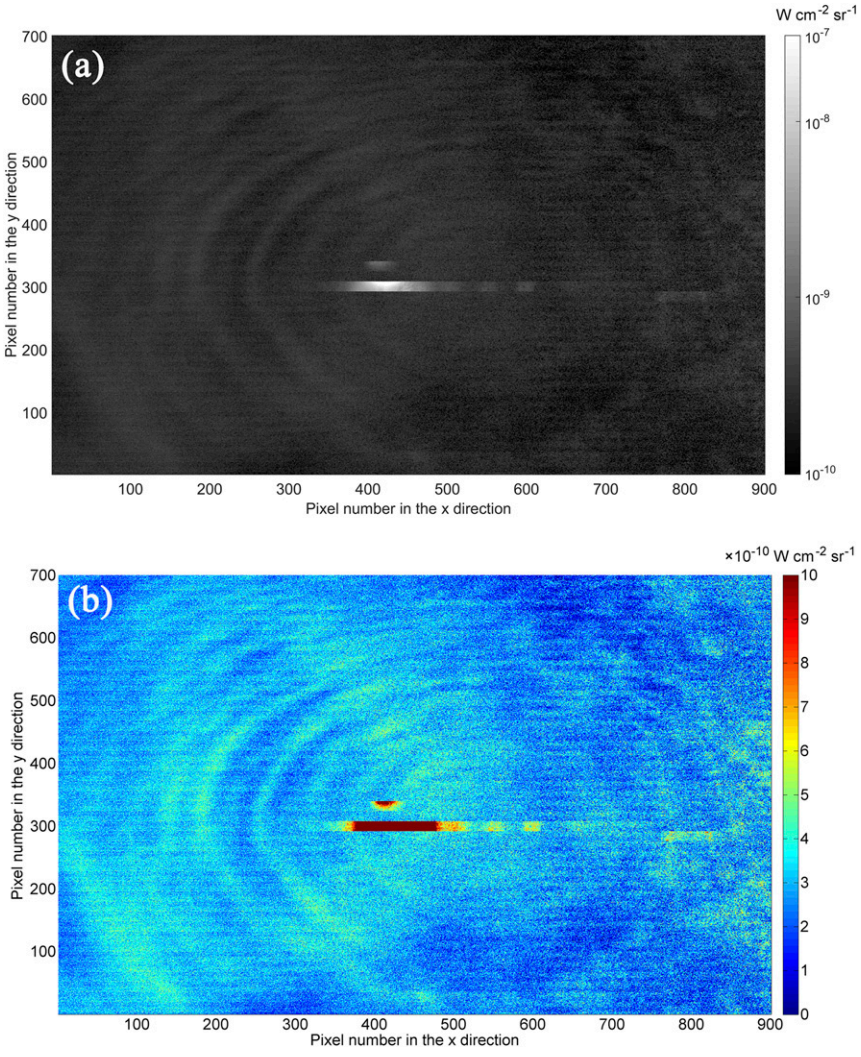

FIG. 7. The local DNB data intercepted on 13 May: (a) the grayscale image after logarithmic operation on radiance and (b) the pseudocolor image.

From Fig. 7 we can see that the selected data reveal obvious features of concentric gravity waves, and there are two bright streaks caused by lightning in the middle. The upper streak is shorter, while the lower one is much longer, spanning nearly half of the image.

After a series of similar processing steps, the final 2DST calculation result is shown in Fig. 8. Figure 8a shows the original smoothed radiance perturbation input into the transformation model. Figure 8b is the real amplitude of the data. The reconstructed gravity waves generally reveal the image characteristics of concentric gravity waves. Figure 8c is the distribution of the absolute amplitude. It can be seen that the stronger gravity wave features are located left of the center. Figure 8d shows the horizontal wavelength distribution of gravity waves as well as the contour lines of absolute amplitude. The horizontal wavelengths are mainly concentrated in the range of 30–60 km. Figure 8e shows the propagation direction of gravity waves as well as the contour lines of absolute amplitude, in which the distribution of the propagation direction is also generally divided into four parts. In the lower-left and upper-right areas, the angle of the propagation direction is positive, while in the upper-left and lower-right areas of the figure, the angle of the propagation direction is negative, which is consistent with the characteristics of the concentric gravity waves.

Compared with Fig. 6, the gravity waves in Fig. 8 have lower SNR, especially in the right half. As a result, the reconstructed gravity waves in the right half of Fig. 8b hardly connect their lines to form continuous curves. Also, it seems that there are no ripple features near the gravity wave center. Therefore, the distribution of horizontal

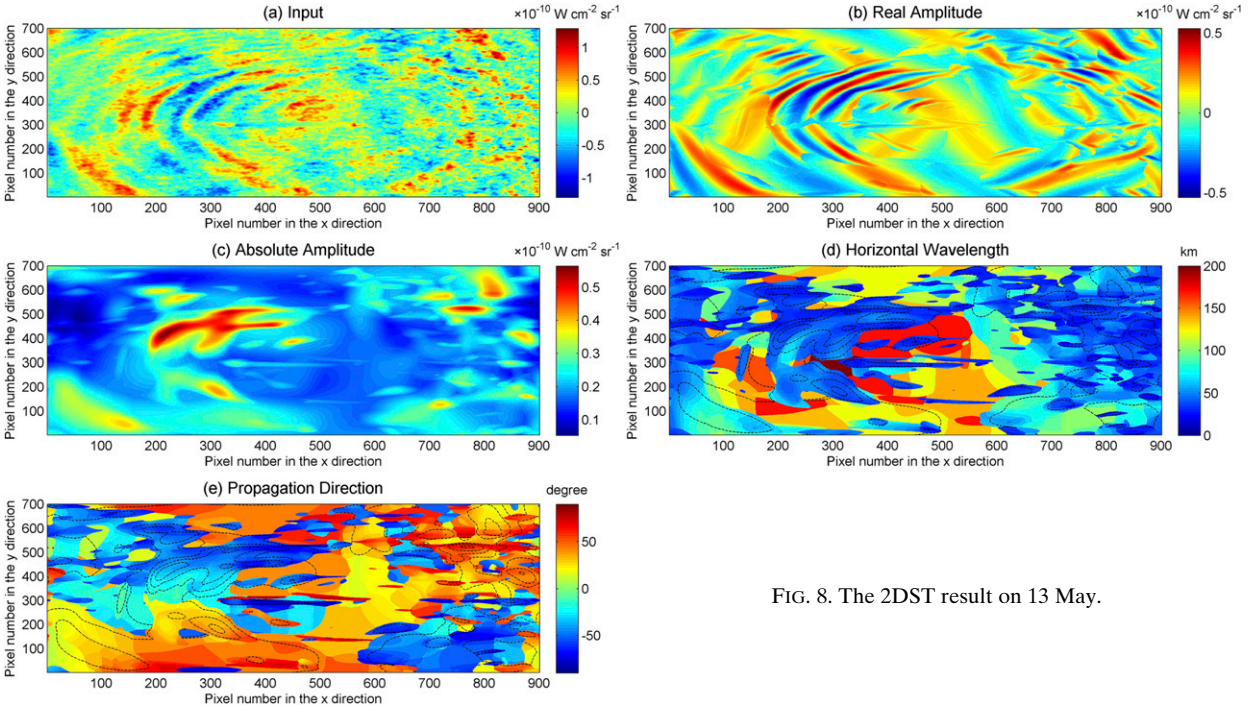

FIG. 8. The 2DST result on 13 May.

wavelength has poorer uniformity in Fig. 8d, causing larger areas to have inaccurate horizontal wavelengths.

5. Conclusions

In this paper we have applied a two-dimensional Stockwell transform technique to airglow measurements from the day–night band of the VIIRS instrument. To our knowledge this study is the first to measure localized mesospheric gravity wave brightness amplitudes, horizontal wavelengths, and propagation directions using such a method and data. We find that the method can characterize the general shape and amplitude of concentric gravity wave patterns, capturing the dominant features and directions with a good degree of accuracy.

As with all observational data, we find that challenges are imposed by the quality of the original image. To this end we have applied an effective method to remove artifacts in our data resulting from lightning and variations in cloud cover, in order to reveal the underlying gravity wave structure.

In practice, we find that while we are able to characterize and localize the gravity wave patterns to first order, these sources of observational error have a significant effect on the measurement of the fine structure of the wave field.

Other caveats include data availability, with the gravity wave detection in the DNB being possible only on moonless nights as a result of the relatively low SNR of wave-induced perturbations in airglow.

The key strength of our 2DST application is that our approach could be tuned and then automated in the future to process tens of thousands of DNB images, globally characterizing gravity wave parameters in this historically poorly studied layer of the atmosphere.

Acknowledgments. The authors thank NOAA CLASS for making DNB products publicly available. This work was supported by the National Natural Science Foundation of China (Grants 41705007 and 41575028) and the U.K. Natural Environment Research Council (Grant NE/R001391/1).

REFERENCES

Alexander, M. J., and C. Barnet, 2007: Using satellite observations to constrain parameterizations of gravity wave effects for global models. *J. Atmos. Sci.*, **64**, 1652–1665, https://doi.org/10.1175/JAS3897.1.

——, S. D. Eckermann, D. Broutman, and J. Ma, 2009: Momentum flux estimates for South Georgia Island mountain waves in the stratosphere observed via satellite. *Geophys. Res. Lett.*, **36**, 1179–1179, https://doi.org/10.1029/2009GL038587.

——, and Coauthors, 2010: Recent developments in gravity-wave effects in climate models and the global distribution of gravity-wave momentum flux from observations and models. *Quart. J. Roy. Meteor. Soc.*, **136**, 1103–112, https://doi.org/10.1002/qj.637.

Azeem, I., J. Yue, L. Hoffmann, S. D. Miller, W. C. Straka, and G. Crowley, 2015: Multisensor profiling of a concentric gravity wave event propagating from the troposphere to the ionosphere. *Geophys. Res. Lett.*, **42**, 7874–7880, https://doi.org/10.1002/2015GL065903.

Bankert, R. L., J. E. Solbrig, T. F. Lee, and S. D. Miller, 2011: Automated lightning flash detection in nighttime visible satellite data. *Wea. Forecasting*, **26**, 399–408, https://doi.org/10.1175/WAF-D-10-05002.1.

Chan, T. F., and J. Shen, 2001: Nontexture inpainting by curvature-driven diffusions. *J. Visual Commun. Image Representation*, **12**, 436–449, https://doi.org/10.1006/jvci.2001.0487.

Dudhia, J., 1993: A nonhydrostatic version of the Penn State–NCAR mesoscale model: Validation tests and simulation of an Atlantic cyclone and cold front. *Mon. Wea. Rev.*, **121**, 1493–1513, https://doi.org/10.1175/1520-0493(1993)121<1493:ANVOTP>2.0.CO;2.

Fritts, D. C., and M. J. Alexander, 2003: Gravity wave dynamics and effects in the middle atmosphere. *Rev. Geophys.*, **41**, 1003, https://doi.org/10.1029/2001RG000106.

——, D. M. Riggin, B. B. Balsley, and R. G. Stockwell, 1998: Recent results with an MF radar at McMurdo, Antarctica: Characteristics and variability of motions near 12-hour period in the mesosphere. *Geophys. Res. Lett.*, **25**, 297–300, https://doi.org/10.1029/97GL03702.

Geller, M. A., and Coauthors, 2013: A comparison between gravity wave momentum fluxes in observations and climate models. *J. Climate*, **26**, 6383–6405, https://doi.org/10.1175/JCLI-D-12-00545.1.

Hillger, D., and Coauthors, 2013: First-light imagery from Suomi NPP VIIRS. *Bull. Amer. Meteor. Soc.*, **94**, 1019–1029, https://doi.org/10.1175/BAMS-D-12-00097.1.

Hindley, N. P., N. D. Smith, C. J. Wright, D. A. S. Rees, and N. J. Mitchell, 2016: A two-dimensional Stockwell transform for gravity wave analysis of AIRS measurements. *Atmos. Meas. Tech.*, **9**, 2545–2565, https://doi.org/10.5194/amt-9-2545-2016.

Hoffmann, L., X. Xue, and M. J. Alexander, 2013: A global view of stratospheric gravity wave hotspots located with Atmospheric Infrared Sounder observations. *J. Geophys. Res. Atmos.*, **118**, 416–434, https://doi.org/10.1029/2012JD018658.

Holton, J. R., 1983: The influence of gravity wave breaking on the general circulation of the middle atmosphere. *J. Atmos. Sci.*, **40**, 2497–2507, https://doi.org/10.1175/1520-0469(1983)040<2497:TIOGWB>2.0.CO;2.

Hu, S., S. Ma, W. Yan, W. Lu, and X. Zhao, 2018: Feasibility of a specialized ground light source for night-time low-light calibration. *Int. J. Remote Sens.*, **39**, 2543–2559, https://doi.org/10.1080/01431161.2018.1430915.

Kim, S. Y., H. Y. Chun, and D. L. Wu, 2009: A study on stratospheric gravity waves generated by Typhoon Ewiniar: Numerical simulations and satellite observations. *J. Geophys. Res.*, **114**, D22104, https://doi.org/10.1029/2009JD011971.

Kuester, M., M. Alexander, and E. Ray, 2008: A model study of gravity waves over Hurricane Humberto (2001). *J. Atmos. Sci.*, **65**, 3231–3246, https://doi.org/10.1175/2008JAS2372.1.

Lai, C., J. Yue, J. Xu, W. C. Straka, S. D. Miller, and X. Liu, 2017: Suomi NPP VIIRS/DNB imagery of nightglow gravity waves from various sources over China. *Adv. Space Res.*, **59**, 1951–1961, https://doi.org/10.1016/j.asr.2017.01.041.

Ma, S., W. Yan, Y. X. Huang, W. H. Ai, and X. Zhao, 2015: Vicarious calibration of S-NPP/VIIRS day–night band using deep convective clouds. *Remote Sens. Environ.*, **158**, 42–55, https://doi.org/10.1016/j.rse.2014.11.006.

——, ——, Y. Huang, J. Jiang, S. Hu, and Y. Wang, 2016: Calibration method of low-light sensor based on bridge lights. *J. Atmos. Oceanic Technol.*, **33**, 1123–1134, https://doi.org/10.1175/JTECH-D-15-0225.1.

Mansinha, L., R. Stockwell, R. Lowe, M. Eramian, and R. Schincariol, 1997: Local S-spectrum analysis of 1-D and 2-D data. *Phys. Earth Planet. Inter.*, **103**, 329–336, https://doi.org/10.1016/S0031-9201(97)00047-2.

Miller, S. D., C. L. Combs, S. Q. Kidder, and T. F. Lee, 2012: Assessing moonlight availability for nighttime environmental applications by low-light visible polar-orbiting satellite sensors. *J. Atmos. Oceanic Technol.*, **29**, 538–557, https://doi.org/10.1175/JTECH-D-11-00192.1.

——, and Coauthors, 2013: Illuminating the capabilities of the Suomi National Polar-Orbiting Partnership (NPP) Visible Infrared Imaging Radiometer Suite (VIIRS) day/night band. *Remote Sens.*, **5**, 6717–6766, https://doi.org/10.3390/rs5126717.

——, W. C. Straka, J. Yue, S. M. Smith, M. J. Alexander, L. Hoffmann, M. Setvák, and P. T. Partain, 2015: Upper atmospheric gravity wave details revealed in nightglow satellite imagery. *Proc. Natl. Acad. Sci. USA*, **112**, E6728–E6735, https://doi.org/10.1073/pnas.1508084112.

Nishioka, M., T. Tsugawa, M. Kubota, and M. Ishii, 2013: Concentric waves and short-period oscillations observed in the ionosphere after the 2013 Moore EF5 tornado. *Geophys. Res. Lett.*, **40**, 5581–5586, https://doi.org/10.1002/2013GL057963.

Pinnegar, C. R., and L. Mansinha, 2003: The S-transform with windows of arbitrary and varying shape. *Geophysics*, **68**, 381–385, https://doi.org/10.1190/1.1543223.

Plougonven, R., A. Hertzog, and H. Teitelbaum, 2008: Observations and simulations of a large-amplitude mountain wave breaking over the Antarctic Peninsula. *J. Geophys. Res.*, **113**, D16113, https://doi.org/10.1029/2007JD009739.

Rudin, L. I., S. Osher, and E. Fatemi, 1992: Nonlinear total variation based noise removal algorithms. *Proceedings of the Eleventh International Conference of the Center for Nonlinear Studies on Experimental Mathematics: Computational Issues in Nonlinear Science; Computational Issues in Nonlinear Science*, J. M. Hyman, H. Flaschka, and F. H. Busse, Eds., Elsevier, 259–268.

Skamarock, W. C., J. B. Klemp, J. Dudhia, D. O. Gill, D. M. Barker, W. Wang, and J. G. Powers, 2005: A description of the Advanced Research WRF version 2. NCAR Tech. Note NCAR/TN-468+STR, 88 pp., http://dx.doi.org/10.5065/D6DZ069T.

Stockwell, R. G., 1999: S-transform analysis of gravity wave activity from a small scale network of airglow imagers. Ph.D. thesis, University of Western Ontario, 366 pp.

——, L. Mansinha, and R. P. Lowe, 1996: Localization of the complex spectrum: The S transform. *IEEE Trans. Signal Process.*, **44**, 998–1001, https://doi.org/10.1109/78.492555.

Uprety, S., C. Cao, X. Xiong, S. Blonski, A. Wu, and X. Shao, 2013: Radiometric intercomparison between *Suomi-NPP* VIIRS and *Aqua* MODIS reflective solar bands using simultaneous nadir overpass in the low latitudes. *J. Atmos. Oceanic Technol.*, **30**, 2720–2736, https://doi.org/10.1175/JTECH-D-13-00071.1.

Wu, D. L., 2004: Mesoscale gravity wave variances from AMSU-A radiances. *Geophys. Res. Lett.*, **31**, L12114, https://doi.org/10.1029/2004GL019562.

Yue, J., S. D. Miller, L. Hoffmann, and W. C. Straka, 2014: Stratospheric and mesospheric concentric gravity waves over tropical cyclone Mahasen: Joint AIRS and VIIRS satellite observations. *J. Atmos. Sol.-Terr. Phys.*, **119**, 83–90, https://doi.org/10.1016/j.jastp.2014.07.003.